Materials Advances

ROYAL SOCIETY OF CHEMISTRY

PAPER

View Article Online
View Journal | View Issue

Cite this: *Mater. Adv.*, 2025, **6**, 4672

Phase transition of $(CH_3)_2CHNH_3CuCl_3$: crystal growth, crystal structure, coordination geometry, and molecular motion†

Hyunje Park[b] and Ae Ran Lim *[ab]

Received 24th January 2025,
Accepted 3rd June 2025

DOI: 10.1039/d5ma00063g

rsc.li/materials-advances

The single crystals of $(CH_3)_2CHNH_3CuCl_3$ were grown, and their phase transition temperature was determined to be 341 K (T_C) through differential scanning calorimetry and powder X-ray diffraction. Additionally, the structures of the single crystals were examined *via* single-crystal X-ray diffraction at 300 K (phase II, below T_C) and 350 K (phase I, above T_C). The sample underwent a thermochromic transition near the T_C, changing from a low-temperature brown material to a high-temperature orange material. The phase II and I systems were triclinic ($P\bar{1}$) and orthorhombic (*Pcan*), respectively. The ^{1}H, ^{13}C, and ^{15}N nuclear magnetic resonance (NMR) chemical shifts of the system were monitored to investigate the structural geometry of the $(CH_3)_2CHNH_3$ cations near phase I and II. Abrupt changes were observed in the chemical shifts near the T_C, indicating a first-order phase transition from triclinic to orthorhombic symmetry. The results of this study imply that the structural environments around ^{1}H, ^{13}C, and ^{15}N in the $(CH_3)_2CHNH_3$ cations change significantly during phase II to I transition. Moreover, energy transfer was discussed based on NMR spin–lattice relaxation time data. This study indicates that the structural and physical properties of $(CH_3)_2CHNH_3CuCl_3$, an organic–inorganic material, make it a promising candidate for a wide range of potential applications.

1. Introduction

The effects of external magnetic fields on low-dimensional magnets have garnered significant attention from both experimental and theoretical perspectives. In particular, the critical properties of alternating spin-1/2 chains in magnetic fields have been extensively studied. Rapid progress in the fabrication of antiferromagnetic–ferromagnetic (AF–F) compounds has fueled this interest further. Owing to a gap in their spin excitation spectrum, AF–F chains exhibit interesting quantum behavior when subjected to a magnetic field.[1] A typical example of an AF–F compound comprising alternating ferromagnetic and antiferromagnetic Heisenberg chains with S = 1/2 is organic-inorganic $(CH_3)_2CHNH_3CuCl_3$ (isopropylammonium copper trichloride).[2–18] From the perspective of crystal structure, the origin of the spin gap in AF–F chains is attributed to the S = 1/2 ferromagnetic–antiferromagnetic alternating chains along the *a*-axis in the system. Consequently, AF–F compounds can be described as structures comprising a spin ladder along the *c*-axis consisting of strongly coupled ferromagnetic rungs and an antiferromagnetic chain with an excitation gap of 13.6 K based on neutron inelastic scattering experiments. Meanwhile, similar findings on crystal growth, density functional theory (DFT), and characterization of organic optical materials have been recently reported.[19–21]

$(CH_3)_2CHNH_3CuCl_3$ undergoes a thermochromic phase transition at T_C = 324 K with a color change from brown at low temperatures to orange at high temperatures.[22,23] The most easily detectable solid-state phase transitions are those in which the crystal color changes with temperature. Discontinuous thermochromic phase transitions are characterized by a significant color change at a specific temperature, indicating an abrupt shift in the properties of the crystal at T_C. In transition–metal complexes, thermochromism often indicates a change in ligand coordination. These transformations may involve alterations in atomic connectivity or geometric distortions in chemical structures.[23]

Low-temperature phase II systems adopt a triclinic structure with the space group $P\bar{1}$. However, the lattice parameters reported by Roberts *et al.*[23] are a = 11.692 Å, b = 7.804 Å, c = 6.106 Å, α = 79.00°, β = 122.60°, and γ = 116.47° with Z = 2, whereas those reported by Manaka *et al.*[2] are α = 97.62°, β = 101.05°, and γ = 67.28°. High-temperature phase I systems are orthorhombic with the space group *Pcan*, and show the following lattice parameters: a = 17.589 Å, b = 7.296 Å, and c = 6.365 Å with Z = 4. In phase II, each Cu^{2+} is located almost at the center

[a] *Graduate School of Carbon Convergence Engineering, Jeonju University, Jeonju 55069, Korea*
[b] *Department of Science Education, Jeonju University, Jeonju 55069, Korea. E-mail: aeranlim@hanmail.net, arlim@jj.ac.kr*

† Electronic supplementary information (ESI) available. CCDC 2419287 and 2419289. For ESI and crystallographic data in CIF or other electronic format see DOI: https://doi.org/10.1039/d5ma00063g

of the base of a pyramid comprising five Cl^- ions, and adjacent pyramids are inverted. Thus, the phase II structure consists of bibridged linear chains of Cu_2Cl_6 dimers, whereas the phase I structure comprises tribridged chains of $CuCl_3$ dimers. The $(CH_3)_2CHNH_3$ cations are ordered in phase II, but become disordered in phase I.[23]

The heat transport properties of the spin-gap material $(CH_3)_2CHNH_3CuCl_3$ at ultra-low temperatures and under high magnetic fields are discussed in the literature.[14] The temperature dependencies of the gap energies and magnon lifetimes are measured using quasi-one-dimensional $S = 1/2$ gapped quantum magnets using inelastic neutron scattering.[12] Additionally, inelastic neutron scattering and bulk magnetic susceptibility measurements of the quantum $S = 1/2$ spin ladder system $(CH_3)_2CHNH_3CuCl_3$ have been conducted under hydrostatic pressure.[24] Nuclear magnetic resonance (NMR) studies on ^1H and ^{35}Cl were conducted at low temperatures below T_N = 13.5 K.[25–29] The temperature dependence of optical linear birefringence in the AF–F state has also been measured.[30] However, studies on the thermodynamic properties and molecular motions of the $(CH_3)_2CHNH_3$ cations in $(CH_3)_2CHNH_3CuCl_3$ near the phase transition temperature of the system are scarce.

In this study, single crystals of $(CH_3)_2CHNH_3CuCl_3$ were grown and their phase transition temperatures were determined using differential scanning calorimetry (DSC) and X-ray diffraction (XRD) experiments with powder samples. Additionally, the structures of the single crystals above and below the phase transition temperature, corresponding to phases I and II, were examined *via* single-crystal XRD at 350 and 300 K, respectively. Moreover, the thermal properties of the system are briefly discussed. To investigate the influence of $(CH_3)_2CHNH_3$ cations near phase I and II, the temperature dependence of the chemical shifts in the ^1H, ^{13}C, and ^{15}N NMR spectra of the synthesized system was analyzed. Abrupt shifts were observed in phase I and II near 340 K, indicating a transition from triclinic to orthorhombic symmetry. In addition, the energy transfer, indicated by NMR spin–lattice relaxation time ($T_{1\rho}$) data, was examined to highlight the contribution of $(CH_3)_2CHNH_3$ cations toward the properties of $(CH_3)_2CHNH_3CuCl_3$. Through DSC, TGA, and NMR measurements, we want to understand the thermal stability and molecular motion of this material as a result of its physicochemical properties, enabling the development of high-efficiency and highly stable materials.

2. Experimental

2.1. Crystal growth

High-quality single crystals of $(CH_3)_2CHNH_3CuCl_3$ were grown through the slow evaporation method using a mixture containing $(CH_3)_2CHNH_2{\cdot}HCl$ and $CuCl_2$ in a 1 : 1 ratio of 15 g and 21.10 g, respectively, in ethanol. After stirring and heating to saturation, single crystals were grown from it *via* gradual evaporation for several weeks in a constant-temperature bath at 297 K. The flat, rectangular, dark-brown crystals with a size of up to $15 \times 5 \times 1$ mm^3 were stored in a desiccator to prevent moisture-related degradation.

2.2. Characterization

A TA Instruments DSC (Model 25) system with temperature increment and heating rates of 10 °C min^{-1} over a temperature range of 200–570 K under a dry nitrogen gas flow was used for DSC measurements. The crystal morphology and its variations with temperature were observed using an optical polarizing microscope (Carl Zeiss) on a hot stage (Linkam THMS 600). In addition, thermogravimetric (TG) analysis was conducted over a temperature range of 300–973 K under a nitrogen atmosphere at a temperature-increment rate of 10 °C min^{-1}. Fourier transform infrared (FT-IR) spectra were measured within 4000–500 cm^{-1} on a PerkinElmer (L1600300) spectrometer using a compressed KBr pellet.

The structures and lattice parameters of the crystals at 300 and 350 K were determined using single-crystal XRD (SCXRD) experiments conducted at the Korea Basic Science Institute (KBSI), Seoul Western Centre. A Bruker SMART CCD diffractometer utilizing graphite-monochromated Mo-Kα radiation and a nitrogen cold stream at −50 °C was used for SCXRD. SMART APEX3 and SAINT were used for data collection and integration, whereas the multiscan method implemented in SADABS was used for absorption corrections. The crystal structure was solved by direct methods and refined using full-matrix least squares on F^2 using the SHELXTL program.[31] All non-hydrogen atoms were refined anisotropically, and hydrogen atoms were positioned at their idealized geometric locations. In addition, powder XRD (PXRD) patterns were recorded at several temperatures using an XRD system with a Mo-Kα radiation source, similar to the system used for SCXRD.

The NMR spectra of $(CH_3)_2CHNH_3CuCl_3$ were recorded using a 400 MHz NMR spectrometer (Bruker, Germany) at the KBSI, and $T_{1\rho}$ data were recorded on a 500 MHz NMR spectrometer (Bruker, Germany) at the Laboratory of NMR, NCIRF, Seoul National University. ^1H magic angle spinning (MAS) NMR experiments were conducted at a Larmor frequency of 400.13 and 500.13 MHz, whereas ^{13}C MAS NMR experiments were conducted at a Larmor frequency of 100.61 and 125.77 MHz. The ^1H and ^{13}C chemical shifts were referenced to tetramethylsilane (TMS). ^{15}N MAS NMR spectra were recorded at a Larmor frequency of 40.54 MHz, and NH_4NO_3 was used as the standard. During experimentation, powdered samples were placed in a 4-mm CP/MAS tube, and magic-angle spinning speeds of 5 and 10 kHz were used to minimize spinning sidebands. The one-dimensional ^1H and ^{13}C NMR spectra were recorded at a delay time of 0.5 s. The ^1H and ^{13}C $T_{1\rho}$ values were measured with delay times ranging from 1 ms to 5 s, and 90° pulses for ^1H and ^{13}C were set to 3.2 and 6.5 μs, respectively. NMR experiments were conducted by lowering the temperature from 300 K to 180 K, and then increasing the temperature again from 180 K to 420 K.

3. Results and discussion

3.1. Phase transition temperature and thermodynamic properties

For DSC experiment, powdered $(CH_3)_2CHNH_3CuCl_3$ single crystals, utilizing a sample mass of 7.5 mg were subjected to a temperature increment at the rate of 10 °C min^{-1}. As shown in

Fig. 1, a small endothermic peak during the heating step was obtained at 341 K with an enthalpy value of 3.52 kJ mol^{-1}, and a large peak was obtained near 469 K. The small peak observed at 341 K corresponds to the phase transition temperature, and the peak at 469 K indicates the melting point. The phase change occurring at this temperature was later confirmed using SCXRD and PXRD. Here, the temperature range below 341 K was classified as phase II and the region above 341 K was classified as phase I. Changes in the state of the single crystal with temperature, observed using a polarizing microscope, are shown in the inset of Fig. 1. Below 345 K, the single crystal is dark brown (Fig. 1(a)–(c)), and above 345 K, which is near the phase transition temperature, the color of the single crystal is slightly orange (Fig. 1(d)). In addition, at ~469 K, a small bubble appears on the right side of the single crystal (Fig. 1(e) and (f)), consistent with the DSC results, and the crystal begins melting. Near 490 K (Fig. 1(g)), the crystal melts. Thus, both DSC and polarizing microscopy experiments indicated a thermochromic phase transition from dark-brown to dark-orange at 340 K and single-crystal melting at 469 K. Even though the color of the single crystal changes above T_C, the coexistence of orange and black phases is observed. Detailed images of the single crystal are shown in the supplementary data S1 (ESI†). Additionally, the single crystal was maintained at 350 K and the change over time was observed. After 1 min, the color immediately changed to dark orange and remained dark orange until 100 min. These results are represented in supplementary data S2 (ESI†).

Similar to DSC, TG experiments were conducted with the sample of 6.7 mg over a temperature range of 300–873 K at a heating rate of 10 °C min^{-1} (Fig. 2). TG analysis showed that the crystals were thermally stable up to 461 K with a weight loss of 2%; at 461 K, partial decomposition began to occur. In addition, the TG curve decreased significantly over two stages, and only ~10% of the residue remained at temperatures above 850 K. In particular, the inflection point near 585 K in the TG curve

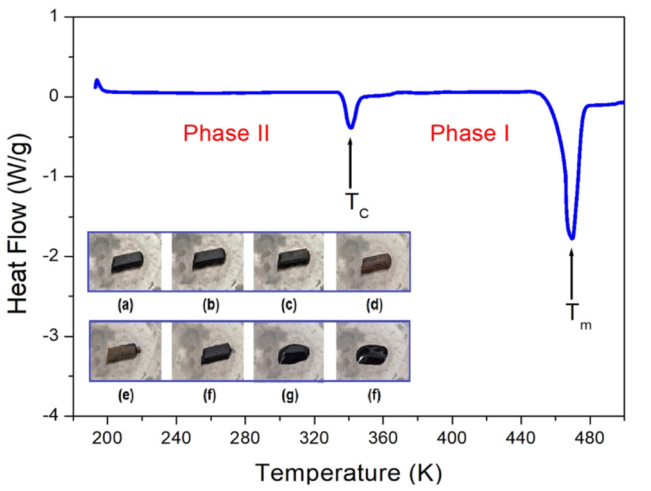

Fig. 1 DSC curve of $(CH_3)_2CHNH_3CuCl_3$ during heating at 10 °C min^{-1} (Inset: Morphology of a single crystal at (a) 300 K, (b) 330 K, (c) 345 K, (d) 360 K, (e) 460 K, (f) 475 K, (g) 490 K, and (f) 500 K, as observed by optical polarizing microscopy).

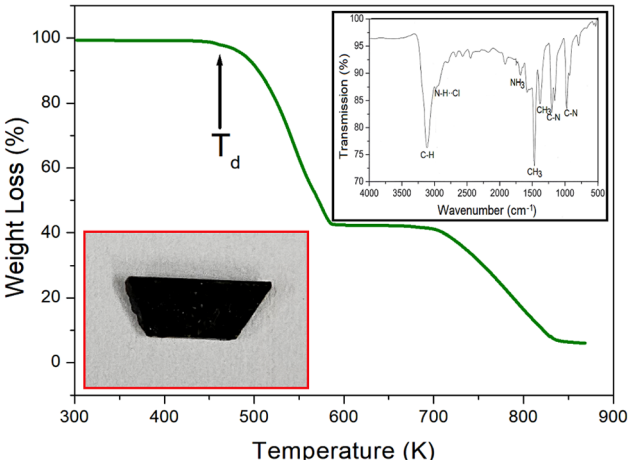

Fig. 2 TG curve of $(CH_3)_2CHNH_3CuCl_3$ during heating at 10 °C min^{-1}. T_d indicates the decomposition temperature. (Inset: Morphology of a single crystal and FT-IR spectrum of $(CH_3)_2CHNH_3CuCl_3$ within 4000–500 cm^{-1} at 300 K).

corresponds to a weight loss of 60%, which is due to the decomposition of $(CH_3)_2CHNH_3Cl$; this can almost entirely be attributed to the decomposition of organic matter.

FT-IR spectrum recorded within 4000–500 cm^{-1} at room temperature are shown in the inset of Fig. 2. The very strong peak near 3116 cm^{-1} corresponds to the C–H mode, the weak and broad peak at 3000 cm^{-1} corresponds to the N–H···Cl hydrogen bond, the very small peak at 1683 cm^{-1} corresponds to NH_3, the spectral peaks at 1468 and 1382 cm^{-1} correspond to CH_3, and the peaks near 1202 and 975 cm^{-1} correspond to the C–N mode.

3.2. X-ray diffraction experiments on single-crystals and powder

The crystal structure and lattice parameters were determined by SCXRD experiments with single crystals of $(CH_3)_2CHNH_3CuCl_3$ at 300 and 350 K. In phase II of 300 K, the crystal structure exhibited a triclinic structure with the space group $P\bar{1}$ and the following lattice parameters: a = 6.1124 Å, b = 7.8109 Å, c = 9.7517 Å, α = 67.3010°, β = 82.3850°, γ = 79.0490°, and Z = 2. In phase I of 350 K, the crystal structure showed orthorhombic symmetry with the space group *Pbcn* and the following lattice constants: a = 6.3635 Å, b = 17.6055 Å, c = 7.2977 Å, $\alpha = \beta = \gamma$ = 90°, and Z = 4. The detailed SCXRD results at 300 and 350 K are listed in Table 1. The triclinic structure and numbering of atoms in phase II at 300 K are shown in Fig. 3(a) and (b), respectively. The orthorhombic structure and numbering of atoms at 350 K in phase I are shown in Fig. 4(a) and (b), respectively. The bond lengths and angles at 300 and 350 K are listed in Tables 2 and 3. The bond-lengths of N–H···Cl hydrogen bond at 300 K and 350 K are 3.806 Å and 3.489 Å, respectively. Single crystals of the synthesized sample were confirmed to comprise $(CH_3)_2CHNH_3$ cations and $CuCl_3$ anions, with Cu atoms surrounded by Cl atoms. Fig. 3 shows that the anionic structure of phase II consists of nearly planar Cu_2Cl_6 dimers linked by long axial Cu–Cl bonds, forming bibridged linear chains along the *c*-axis. The Cu is surrounded by five Cl atoms in a nearly square pyramidal arrangement.

Table 1 Crystal data and structure refinement for $(CH_3)_2CHNH_3CuCl_3$ at 300 K and 350 K

Temperature	300 K	350 K
Chemical formula	$C_3H_{10}NCuCl_3$	$C_3H_{10}NCuCl_3$
Weight	230.01	230.01
Crystal system	Triclinic	Orthorhombic
Space group	$P\bar{1}$	*Pbcn*
a (Å)	6.1124 (2)	6.3635 (2)
b (Å)	7.8109 (3)	17.6055 (9)
c (Å)	9.7517 (4)	7.2977 (3)
α (°)	67.3010 (10)	90
β (°)	82.3850 (10)	90
γ (°)	79.0490 (10)	90
Z	2	4
V (Å^3)	420.79 (3)	817.58 (17)
Density (calculated)(Mg m^{-3})	1.815	1.869
Absorption coefficient (mm^{-1})	3.457	3.559
F(000)	230	460
Crystal size (mm^3)	0.410 × 0.146 × 0.135	0.204 × 0.173 × 0.113
Theta range for data collection (°)	2.860 to 28.314	3.951 to 28.250
Index ranges	$-8 \le h \le 8$, $-10 \le k \le 10$, $-13 \le l \le 13$	$-9 \le h \le 9$, $-23 \le k \le 23$, $-8 \le l \le 8$
Completeness to theta = 25.242° (%)	99.9	98.7
Max and min transmission	0.7457 and 0.6480	0.7457 and 0.6396
Data/restraints/parameters	2092/0/76	1011/2/44
Radiation type	Mo-Kα	Mo-Kα
Wavelength (Å)	0.71073	0.71073
Reflections collected	15 685	8240
Independent reflections	2092 (R_{int} = 0.0294)	1011 (R_{int} = 0.0208)
Goodness-of-fit on F^2	1.102	1.116
Final R indices [$I > 2$ Sigma(I)]	R_1 = 0.0167, wR_2 = 0.0430	R_1 = 0.0205, wR_2 = 0.0559
R indices (all data)	R_1 = 0.0194, wR_2 = 0.0441	R_1 = 0.0236, wR_2 = 0.0581
Extinction coefficient	0.065(2)	n/a
Largest diff. peak and hole (e Å^{-3})	0.323 and −0.232	0.314 and −0.379

In the high – temperature phase, the crystal structure changes from a bibridged chain of dimers to a tribridged chain. The crystal structure consists of linear chains of face-covalent $CuCl_3$ linked by hydrogen bonds to $(CH_3)_2CHNH_3$ cations. During phase II to I transition, the *b*-axis elongates and $CuCl_3$ is aligned along the *c*-axis. Notably, the triclinic structure in phase II with C1, C2, and C3 in different environments at 300 K changes to an orthorhombic structure with improved symmetry owing to C1 and C2 in different environments at 350 K in phase I. Therefore, the symmetry of the $(CH_3)_2CHNH_3$ ions is higher in phase I than in phase II. Crystallographic data at 300 and 350 K, including the CIF files, were deposited at the Cambridge Crystallographic Data Center (CCDC 2419287, 2419289†).

Simulated PXRD patterns based on the CIF data of the crystal structures at 300 and 350 K are shown in Fig. 5. The patterns corresponding to phase I and II are completely different owing to structural differences in both phases. The strongest peak in phase II is observed at (001), whereas that in phase I is observed at (020). The Mercury software was used for peak reflection. Crushed single crystal samples were used for PXRD experiments over the 2θ range of 8–55° above 300 K including the simulated powder patterns in 300 and 350 K, as shown in Fig. 6. The same peaks were consistently observed in the PXRD patterns recorded below 340 K, but a change in the peak pattern was observed in spectra recorded above 340 K, consistent with the endothermic peak observed at 341 K in the DSC results. Notably, spectra recorded above 460 K did not contain any peaks corresponding to a crystalline structure, consistent with the melting of the single crystal. Consequently, based on DSC, SCXRD, and PXRD analyses, 341 K was identified as the phase transition temperature. On the other hand, the PXRD peaks at 350 K exhibit a coexistence of peaks from both phase I and II, primarily in the low-angle region, as indicated by the ellipses in Fig. 6. A more detailed figure was presented in supplementary data S3 (ESI†).

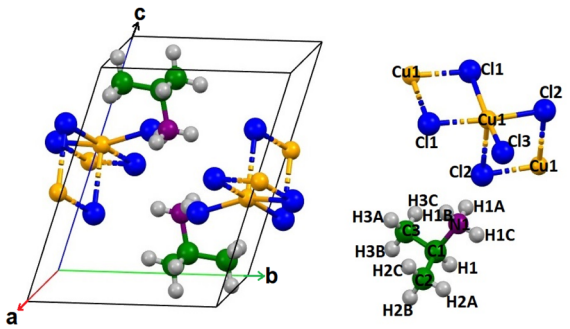

Fig. 3 The triclinic structure and numbering of atoms in a $(CH_3)_2CHNH_3CuCl_3$ crystal at 300 K (A. R. Lim CCDC 2419287†).

3.3. ^{1}H MAS NMR chemical shifts and spin–lattice relaxation time

The NMR spectra of $(CH_3)_2CHNH_3CuCl_3$ crystals, recorded using MAS NMR at a frequency of 400.13 MHz under a magnetic field of 9.4 T, were analyzed to understand the structural geometry of ^{1}H near the T_C. Complex spectra were recorded owing to the chemical shift distribution and anisotropy at numerous nonequivalent proton sites in the $(CH_3)_2CHNH_3$ group. The ^{1}H NMR spectra of phase II and I below and above the T_C, respectively, are

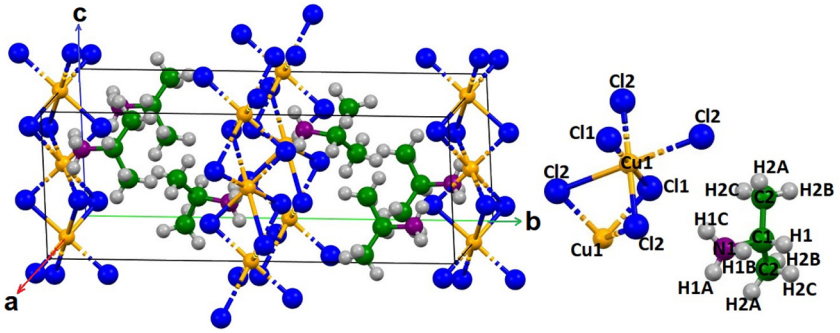

Fig. 4 The orthorhombic structure and numbering of atoms in a $(CH_3)_2CHNH_3CuCl_3$ crystal at 350 K (A. R. Lim CCDC 2419289†).

Table 2 The bond-lengths (Å) and bond-angles (°) for $(CH_3)_2CHNH_3CuCl_3$ at 300 K

Bond-lengths		Bond-angles		Bond-angles	
Cu(1)–Cl(2)	2.2709(4)	Cl(2)–Cu(1)–Cl(3)	93.208(14)	N(1)–C(1)–C(2)	108.42(14)
Cu(1)–Cl(3)	2.2722(4)	Cl(2)–Cu(1)–Cl(1)	90.925(14)	N(1)–C(1)–C(3)	108.73(14)
Cu(1)–Cl(1)	2.3033(4)	Cl(3)–Cu(1)–Cl(1)	160.430(18)	C(2)–C(1)–C(3)	113.36(16)
Cu(1)–Cl(1)#1	2.3168(4)	Cl(2)–Cu(1)–Cl(1)#1	175.085(15)	N(1)–C(1)–H(1)	108.8
Cu(1)–Cl(2)#2	2.7040(4)	Cl(3)–Cu(1)–Cl(1)#1	90.587(14)	C(2)–C(1)–H(1)	108.8
N(1)–C(1)	1.504(2)	Cl(1)–Cu(1)–Cl(1)#1	84.469(14)	C(3)–C(1)–H(1)	108.8
N(1)–H(1A)	0.8900	Cl(2)–Cu(1)–Cl(2)#2	90.687(13)	C(1)–C(2)–H(2A)	109.5
N(1)–H(1B)	0.8900	Cl(3)–Cu(1)–Cl(2)#2	98.506(14)	C(1)–C(2)–H(2B)	109.5
N(1)–H(1C)	0.8900	Cl(1)–Cu(1)–Cl(2)#2	100.565(15)	H(2A)–C(2)–H(2B)	109.5
C(1)–C(2)	1.508(2)	Cl(1)#1–Cu(1)–Cl(2)#2	91.840(15)	C(1)–C(2)–H(2C)	109.5
C(1)–C(3)	1.516(2)	Cu(1)–Cl(2)–Cu(1)#2	89.313(13)	H(2A)–C(2)–H(2C)	109.5
C(1)–H(1)	0.9800	Cu(1)–Cl(1)–Cu(1)#1	95.531(14)	H(2B)–C(2)–H(2C)	109.5
C(2)–H(2A)	0.9600	C(1)–N(1)–H(1A)	109.5	C(1)–C(3)–H(3A)	109.5
C(2)–H(2B)	0.9600	C(1)–N(1)–H(1B)	109.5	C(1)–C(3)–H(3B)	109.5
C(2)–H(2C)	0.9600	H(1A)–N(1)–H(1B)	109.5	H(3A)–C(3)–H(3B)	109.5
C(3)–H(3A)	0.9600	C(1)–N(1)–H(1C)	109.5	C(1)–C(3)–H(3C)	109.5
C(3)–H(3B)	0.9600	H(1A)–N(1)–H(1C)	109.5	H(3A)–C(3)–H(3C)	109.5
C(3)–H(3C)	0.9600	H(1B)–N(1)–H(1C)	109.5	H(3B)–C(3)–H(3C)	109.5
H(1A)–Cl(3)	2.916				

Table 3 The bond-lengths (Å) and bond-angles (°) for $(CH_3)_2CHNH_3CuCl_3$ at 350 K

Bond-lengths		Bond-angles		Bond-angles	
Cu(1)–Cl(2)#1	2.2915(4)	Cl(2)#1–Cu(1)–Cl(2)	180.0	C(2)–C(1)–N(1)	109.6(2)
Cu(1)–Cl(2)	2.2915(4)	Cl(2)#1–Cu(1)–Cl(1)	90.878(13)	C(2)–C(1)–H(1)	105.3
Cu(1)–Cl(1)	2.3384(4)	Cl(2)–Cu(1)–Cl(1)	89.122(13)	N(1)–C(1)–H(1)	105.3
Cu(1)–Cl(1)#1	2.3385(4)	Cl(2)#1–Cu(1)–Cl(1)#1	89.123(13)	C(1)–C(2)–H(2A)	109.5
N(1)–C(1)	1.506(4)	Cl(2)–Cu(1)–Cl(1)#1	90.878(13)	C(1)–C(2)–H(2B)	109.5
N(1)–H(1A)	0.8900	Cl(1)–Cu(1)–Cl(1)#1	180.0	H(2A)–C(2)–H(2B)	109.5
N(1)–H(1B)	0.8900	Cl(1)–Cu(1)–Cl(1)#3	85.738(18)	C(1)–C(2)–H(2C)	109.5
N(1)–H(1C)	0.8900	C(1)–N(1)–H(1A)	109.5	H(2A)–C(2)–H(2C)	109.5
C(1)–C(2)	1.477(3)	C(1)–N(1)–H(1B)	109.5	H(2B)–C(2)–H(2C)	109.5
C(1)–H(1)	0.9800	H(1A)–N(1)–H(1B)	109.5		
C(2)–H(2A)	0.9600	C(1)–N(1)–H(1C)	109.5		
C(2)–H(2B)	0.9600	H(1A)–N(1)–H(1C)	109.5		
C(2)–H(2C)	0.9600	H(1B)–N(1)–H(1C)	109.5		
H(1C)–Cl(2)	2.599				

shown in Fig. 7. NMR experiments at a spinning speed of 5 kHz indicated a sideband distance of 5 kHz (= 12.5 ppm) around the ^{1}H signal, which is similar to the spinning rate. In Fig. 7, the ^{1}H NMR peaks are indicated by arrows. At 300 K, a ^{1}H NMR chemical shift is observed at 10.8 ppm. Only one peak overlaps with the ^{1}H peaks of CH_3, CH, and NH_3. However, the peaks corresponding to NH_3 and CH_3 at 400 K above the T_C are separated to 5.78 and 3.85 ppm, respectively. The sidebands of NH_3 and CH_3 are denoted as x and o, respectively. The ^{1}H NMR chemical shifts with changes in temperature are shown in Fig. 7.

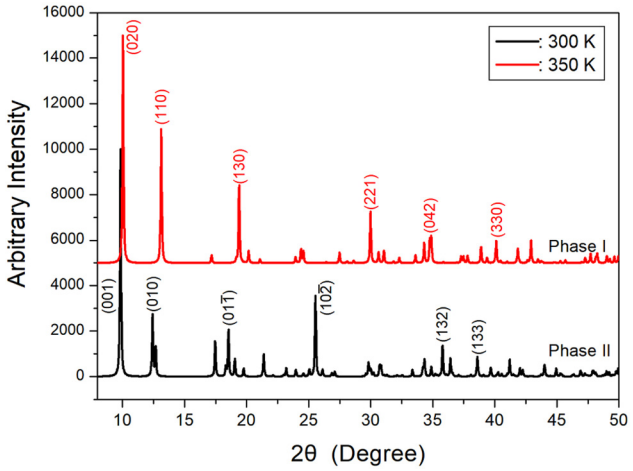

Fig. 5 The simulated powder X-ray diffraction patterns of $(CH_3)_2CHNH_3CuCl_3$ crystals in phase II and I at 300 and 350 K, respectively.

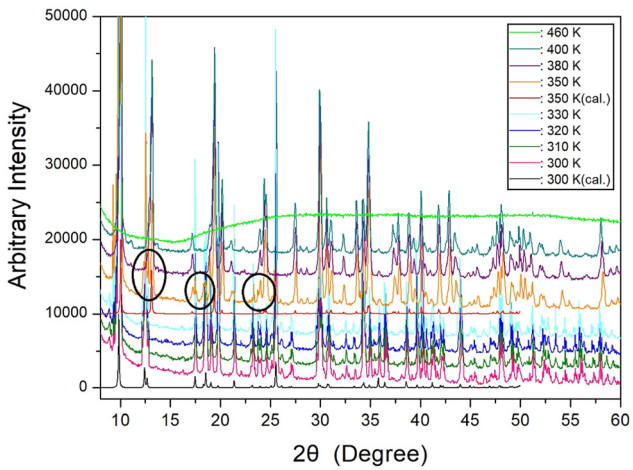

Fig. 6 X-ray diffraction powder patterns of $(CH_3)_2CHNH_3CuCl_3$ near the phase transition temperature including the simulated powder patterns in 300 and 350 K.

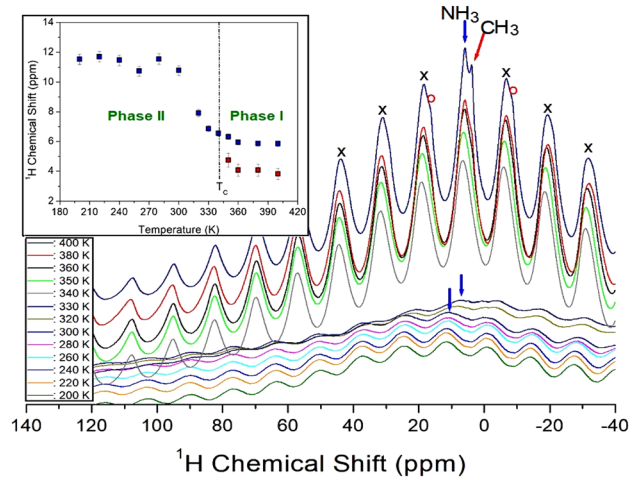

Fig. 7 ^{1}H NMR spectra of $(CH_3)_2CHNH_3CuCl_3$ with increasing temperature at 400.13 MHz. The x and o symbols indicate the sidebands for NH_3 and CH_3, respectively (Inset: ^{1}H NMR chemical shifts in phase II and I).

With increasing temperature, the ^{1}H NMR chemical shifts show an abrupt change with peak splitting in phase I, indicating significant changes in the structural environment around ^{1}H atoms during phase II to I transition. With increasing temperature, the line widths become narrower above T_C, indicating a higher mobility of ^{1}H in phase I than in phase II.

$T_{1\rho}$ values, which represent the extent of energy transfer surrounding the ^{1}H in the $(CH_3)_2CHNH_3$ cation, were estimated to understand the nature of molecular motions in the synthesized system. The intensity changes in the ^{1}H NMR spectra, recorded at various delay times, are characterized by the decay rate of magnetization, which is governed by the $T_{1\rho}$, as follows:[32–35]

$$f(\tau) = f(0)\exp(-\tau/T_{1\rho}), \quad (1)$$

where $f(\tau)$ and $f(0)$ represent the signal intensities at time τ and τ = 0, respectively. The ^{1}H $T_{1\rho}$ value, obtained from the linear slope of the intensity *vs.* delay time plot, determined using eqn (1), was found to be about 8.73 ms at 300 K.

3.4. ^{13}C MAS NMR chemical shifts and spin–lattice relaxation time

^{13}C NMR spectra of $(CH_3)_2CHNH_3CuCl_3$ were recorded using ^{13}C MAS NMR spectroscopy at a frequency of 100.61 MHz and spinning speed of 5 kHz. ^{13}C NMR spectra as a function of temperature are shown in Fig. 8. Using TMS as the standard, the sidebands marked with * are spaced around the ^{13}C signal at 5 kHz (equivalent to 50 ppm), which is consistent with the spinning speed. The ^{13}C NMR peaks are indicated by arrows in Fig. 8(a). Fig. 8(b) shows the temperature dependence of the ^{13}C NMR chemical shifts in phase II and I. Two ^{13}C NMR peaks are observed in both phases, consistent with the presence of ^{13}C in CH and CH_3. The ^{13}C chemical shifts corresponding to CH and CH_3 at 330 K of phase II are observed at 77.16 and 19.19 ppm, respectively, and at 113.35 and 56.52 ppm, respectively, whereas the ^{13}C chemical shifts recorded for CH and CH_3 at 340 K of phase I are obtained at 113.35 and 56.52 ppm, respectively. The discontinuous temperature-dependent changes in ^{13}C chemical shifts near the T_C indicate abrupt changes in the structural geometry around these nuclei, implying that the structural environment around ^{13}C changes significantly during phase II to I transition. Fig. 8(b) shows that with increasing temperature, the line widths above the T_C reduce rapidly from about 12.60 ppm at 200 K to 2.52 ppm at 400 K, indicating a higher mobility of ^{13}C in phase I than in phase II.

The ^{13}C $T_{1\rho}$ for the $(CH_3)_2CHNH_3$ cation was analyzed to understand the nature of molecular motions in $(CH_3)_2CHNH_3CuCl_3$. Variations in the intensity of the ^{13}C NMR spectra were monitored by extending the delay time to 300 K. ^{13}C $T_{1\rho}$ values were determined by modifying the spin-locking pulse sequence applied after cross-polarization (CP). Following CP, ^{13}C magnetization was generated by proton spin-locking. The proton field was then deactivated for a variable period τ,

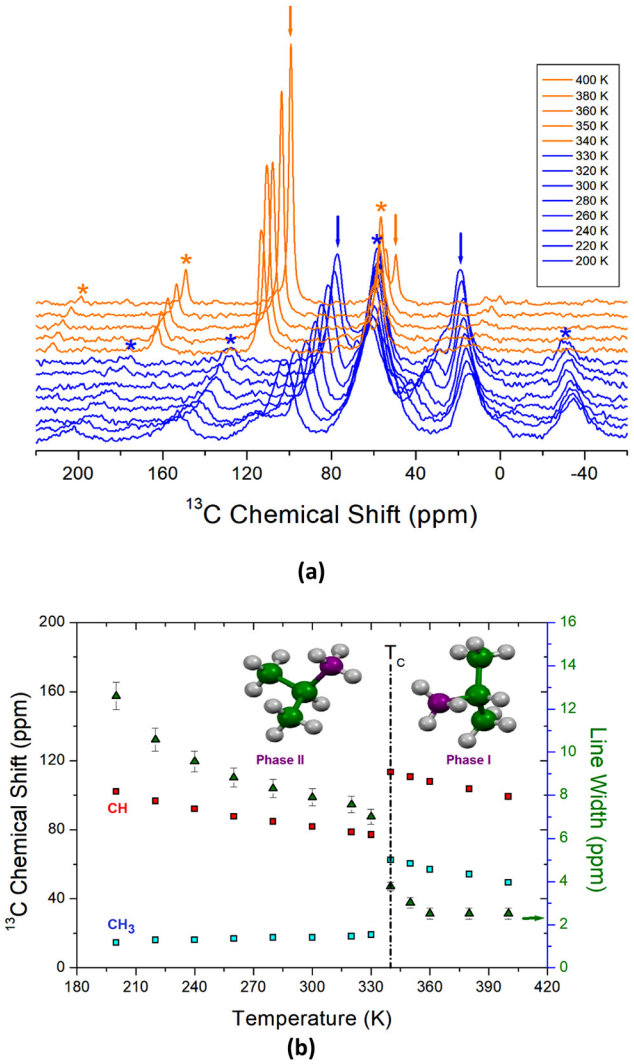

Fig. 8 (a) ^{13}C MAS NMR spectra of $(CH_3)_2CHNH_3CuCl_3$ in phase II and I recorded at 100.61 MHz. The * symbol indicates the sidebands for CH and CH_3, and (b) ^{13}C NMR chemical shifts and line widths of $(CH_3)_2CHNH_3CuCl_3$ in phase II and I.

while the ^{13}C rf field remained active. Subsequently, the free induction decay of ^{13}C was recorded under high-power proton decoupling and subjected to Fourier transformation. Using the same method for obtaining $T_{1\rho}$ in ^{1}H, the values of the ^{13}C $T_{1\rho}$ for CH and CH_3 were determined to be about 99.8 and 55.9 ms, respectively, at 300 K. This result implies that the C atom of CH is bonded with N and H, whereas the C atom of CH_3 is bonded with H; thus, energy transfer is easier in CH_3.

3.5. ^{15}N MAS NMR chemical shifts

^{15}N NMR spectra were measured using MAS NMR at a frequency of 40.54 MHz under a magnetic field of 9.4 T. Although the natural abundance of ^{14}N is higher than that of ^{15}N, the frequency of ^{14}N (26.52 MHz) is lower than that of ^{15}N (40.54 MHz), making it relatively easy to acquire ^{15}N NMR spectra. The ^{15}N NMR spectra of $(CH_3)_2CHNH_3CuCl_3$ as a function of temperature are shown in Fig. 9. Recording ^{15}N

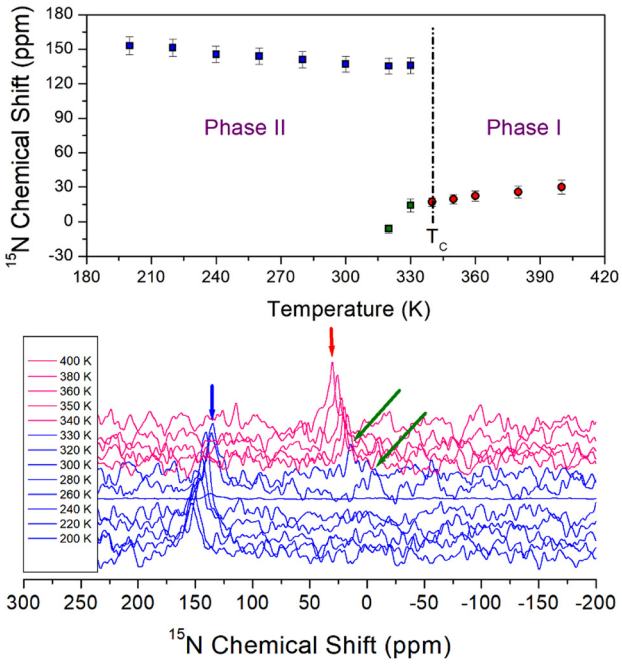

Fig. 9 ^{15}N MAS NMR spectra and chemical shifts of $(CH_3)_2CHNH_3CuCl_3$ in phase II and I at 40.54 MHz. Blue squares and arrows indicate peaks observed in phase II, while red circles and arrows indicate peaks observed in phase I. Here, olive arrows indicate signals suggesting the slight coexistence of the phase II and I states near the T_C.

NMR signals was challenging owing to the low natural abundance of ^{15}N and baseline wiggling. The chemical shifts in this spectrum change abruptly on phase II to I transition. Notably, two signals are observed at 135.84 ppm (marked in blue) and 14.30 ppm (marked in olive) at 330 K, which is slightly below the T_C, indicating the coexistence of phase II and I, while only one signal is observed at 17.06 ppm in phase I at 340 K. There seems to be some coexistence of phase I and II near T_C; the peaks at 350 K in the PXRD are the coexistence of phase I and II, and similarly, the ^{15}N NMR peaks in phase I and II were also observed simultaneously. The abrupt chemical shifts observed in ^{15}N spectra were attributed to changes in the structural geometry of the system, reflecting alterations in the atomic configuration surrounding the ^{15}N nuclei. This abrupt shift in phase I and II near 340 K indicates a transition from triclinic to orthorhombic symmetry.

4. Conclusions

In summary, the phase transition temperature and the melting temperature of $(CH_3)_2CHNH_3CuCl_3$ single crystals were determined to be 341 K (T_C) and 469 K (T_m), respectively, using DSC and PXRD in this study. Additionally, the structures of the single crystals were examined using SCXRD at 300 and 350 K, corresponding to phase II and I. Low-temperature phase II systems showed a triclinic structure with the space group $P\bar{1}$, whereas high-temperature phase I systems showed an orthorhombic structure with the space group *Pcan* with thermodynamic

stability extending up to ~461 K. Meanwhile, the single crystal appeared dark brown at room temperature, but near T_C, a mixture of dark brown and dark orange was observed. This indicates the coexistence of phase I and II near T_C, as confirmed by PXRD experiments and the ^{15}N NMR spectrum. Furthermore, the ^{1}H, ^{13}C, and ^{15}N chemical shifts changed discontinuously near the T_C, and the phase transition was confirmed to be first-order based on NMR results. These results imply that the structural environments around ^{1}H, ^{13}C, and ^{15}N in $(CH_3)_2CHNH_3$ cations change significantly when transitioning from phase II to phase I. Notably, phase transition and ^{1}H and ^{13}C NMR linewidth narrowing occur at the same temperature. The narrowing of linewidths near the T_C is consistent with changes in the free rotation of the cation on phase transition. The structural phase transition can be attributed to changes in the positions of CH_3, CH, and NH_3, which do not affect the magnetic properties. The fundamental mechanism of phase II to I transition in $(CH_3)_2CHNH_3CuCl_3$ crystals indicates that these materials are promising candidates for a wide variety of applications in various fields. Also, understanding their motion through NMR measurements can improve thermal stability and charge transport, enabling the development of high-efficiency and highly stable materials.

Author contributions

A. R. Lim performed the NMR and the x-ray experiments, and wrote the manuscript. H. Park measured the DSC, TGA experiments.

Data availability

Crystallographic data for $(CH_3)_2CHNH_3CuCl_3$ has been deposited at the CCDC 2419287 and 2419289.†

Conflicts of interest

There are no conflicts to declare.

References

1 S. Mahdavifar and A. Akbara, *J. Phys. Soc. Jpn.*, 2008, **77**, 024710.
2 H. Manaka, I. Yamada and K. Yamaguchi, *J. Phys. Soc. Jpn.*, 1997, **66**, 564.
3 H. Manaka and I. Yamada, *J. Mag. Mag. Mater.*, 1998, **177–181**, 681.
4 H. Manaka, I. Yamada, N. V. Mushnikov and T. Goto, *J. Phys. Soc. Jpn.*, 2000, **69**, 675.
5 T. Nakamura, *Prog. Theor. Phys. Suppl.*, 2002, **145**, 353.
6 I. Yamada and H. Manaka, *J. Magn. Magn. Mater.*, 2003, **258–259**, 114.
7 T. Sakai and S. Yamamoto, *Synth. Met.*, 2005, **152**, 477.
8 T. Nakamura, *Phys. Rev. B: Condens. Matter Mater. Phys.*, 2005, **71**, 144401.
9 T. Suzuki, T. Saito, T. Sasaki, A. Oosawa, T. Goto, S. Awaji, K. Watanabe, N. Kobayashi and H. Manaka, *J. Phys.: Conf. Ser.*, 2006, **51**, 187.
10 T. Saito, T. Sasaki, T. Suzuki, A. Oosawa, T. Goto, S. Awaji, K. Watanabe and N. Kobayashi, *J. Phys. Soc. Jpn.*, 2007, **76**, 084708.
11 V. O. Garlea, A. Zheludev, T. Masuda, H. Manaka, L.-P. Regnault, E. Ressouche, B. Grenier, J.-H. Chung, Y. Qiu, K. Kiefer and M. Boehm, *Phys. Rev. Lett.*, 2007, **98**, 167202.
12 A. Zheludev, V. O. Garlea, L.-P. Regnault, H. Manaka, A. Tsvelik and J.-H. Chung, *Phys. Rev. Lett.*, 2008, **100**, 157204.
13 H. Tsujii, Y. H. Kim, Y. Yoshida, Y. Takano, T. P. murphy, K. Kanada, T. Saito, A. Oosawa and T. Goto, *J. Phys.: Conf. Ser.*, 2009, **150**, 42217.
14 Z. Y. Zhao, B. Tong, X. Zhao, L. M. Chen, J. Shi, F. B. Zhang, J. D. Song, S. J. Li, J. C. Wu, H. S. Xu, X. G. Liu and X. F. Sun, *Phys. Rev. B: Condens. Matter Mater. Phys.*, 2015, **91**, 134420.
15 T. Saito, A. Oosawa, T. Goto, T. Suzuki and I. Watanabe, *Phys. Rev. B: Condens. Matter Mater. Phys.*, 2006, **74**, 134423.
16 T. Nakamura, *J. Phys. Soc. Jpn.*, 2003, **72**, 789.
17 B. Nafradi, T. Keller, H. Manaka, A. Zheludev and B. Keimer, *Phys. Rev. Lett.*, 2011, **106**, 177202.
18 H. Manaka, I. Yamada, M. Tokunaga, T. Yasuhira and N. Miura, *Phys. B*, 1998, **246–247**, 513.
19 P. Prabukanthan, V. Bhakyajothi, M. Saravana Kumar, G. Harichandran, K. Dinakaran and P. Seenuvasakumaran, *J. Mol. Struct.*, 2021, **1246**, 131172.
20 P. Prabukanthan, C. Raveendiran, M. Saravana Kumar, G. Harichandran, K. Dinakaran, A. A. Al-Kahtani, M. Ubaidullan, G. Ushanandhini and B. Pandit, *Optik*, 2022, **270**, 170014.
21 P. Prabukanthan, V. Bhakyajothi, K. Dinakaran, S. Uthayakumar and A. Younis, *Chem. Papers*, 2023, **77**, 703.
22 A. Nishimori and M. Sorai, *J. Phys. Chem. Solids*, 1999, **60**, 895.
23 S. A. Roberts, D. R. Bloomquist, R. D. Willett and H. W. Dodgen, *J. Am. Chem. Soc.*, 1981, **103**, 2603.
24 T. Hong, V. O. Garlea, A. Zheludev and J. A. Fernandez-Beca, *Phys. Rev. B: Condens. Matter Mater. Phys.*, 2008, **78**, 224409.
25 K. Kanada, T. Saito, A. Oosawa, T. Goto, T. Suzuki and H. Manaka, *J. Phys. Chem. Solids*, 2007, **68**, 2191.
26 H. Manaka, I. Yamada and W. Higemoto, *J. Phys. Soc. Jpn.*, 2007, **76**, 014704.
27 T. Saito, H. Inoue, J. Tonisi, A. Oosawa, T. Goto, T. Sasaki, N. Kobayasi, S. Awaji and K. Watanabe, *J. Phys.: Conf. Ser.*, 2006, **51**, 203.
28 H. Manaka and I. Yamada, *Phys. B*, 2000, **284–288**, 1607.
29 T. Kubo and T. Waketa, *Phys. B*, 2000, **284–288**, 1609.
30 H. Manaka, I. Yamada, T. Kikuchi, K. Morishita and K. Ilo, *J. Phys. Soc. Jpn.*, 2001, **70**, 2509.
31 *SHELXTL v6.10*, Bruker AXS, Inc., 2000.
32 A. R. Lim, *Sci. Rep.*, 2024, **14**, 11808.
33 A. Abragam, *The Principles of Nuclear Magnetism*, Oxford University Press, 1961.
34 R. K. Harris, *Nuclear Magnetic Resonance Spectroscopy*, Pitman Pub, UK, 1983.
35 J. L. Koenig, *Spectroscopy of Polymers*, Elsevier, New York, 1999.